PAPER

Check for updates

Nitrogen-doped hierarchically porous carbons for non-alkaline Zn–air battery cathodes†

Roman R. Kapaev, [iD] *[a] Yair Shahaf,[b] Masato Sonoo,[ac] Amit Ohayon,[a] David Eisenberg [iD] [b] and Malachi Noked [iD] *[a]

Non-alkaline Zn–air batteries (ZABs) attract great attention because they can potentially combine high energy density, safety, and low cost. However, cathodes for non-alkaline ZABs are underdeveloped and suffer from poor charge–discharge kinetics. Here we study N-doped hierarchically porous carbons, which are synthesized using a self-templating approach, as catalytic scaffolds for oxygen reduction and oxygen evolution reactions (ORR and OER) in near-neutral media. Interestingly, although nitrogen doping does not improve the OER performance or carbon corrosion rate during the OER, it leads to a significant boost of the ORR kinetics in non-alkaline ZABs. Specifically, the reported N-doped hierarchically porous carbons outperform their nitrogen-free hierarchically porous analog, as well as the best commercially available nitrogen-free carbons. These results show that N-doped carbons can serve as promising support materials for non-alkaline ZABs.

Introduction

Zn–air batteries (ZABs) represent a promising type of energy storage devices since they are safe, inexpensive, environmentally friendly and have high theoretical energy density.[1–4] However, the development of long-serving rechargeable ZABs is still a major challenge, although primary alkaline Zn–air cells were commercialized almost a century ago.[5] A conventional ZAB includes a zinc metal anode, an air-breathing cathode, and a strongly alkaline electrolyte, such as 6 M KOH.[1,6] The caustic electrolyte causes corrosion and uneven electrodeposition of Zn, formation of passivating ZnO films, and irreversible formation of K_2CO_3 that clogs the pores of the cathode.[7–10] These problems lead to limited cycle life and decreased energy density of ZABs.

Fortunately, these issues might be circumvented by switching to non-alkaline electrolytes. Using solutions with near-neutral pH suppresses carbonate formation and might enable smooth and reversible plating-stripping of zinc.[10–12] However, slow kinetics of oxygen reduction and oxygen evolution reactions (ORR and OER),

which is associated with low H_3O^+ and OH^- concentrations, limits the applicability of non-alkaline ZABs.[13,14] Therefore, the design of cathode scaffolds that efficiently catalyze ORR and OER in near-neutral media is crucial for the practical implementation of rechargeable ZABs. In contrast to conventional alkaline ZABs that are thoroughly studied, cathodes for the non-alkaline analogs are still underdeveloped.[1]

High and stable catalytic activity can be achieved by using compounds of precious metals, such as Pt for ORR and RuO_x or IrO_x for OER.[15] However, the high price of these elements makes their utilization in ZABs unattractive. Employing single atom catalysts based on abundant transition metals,[15] such as Fe–N–C, may be a more viable approach, but these materials have decreased stability in non-alkaline media because of accelerated metal dissolution induced by Fenton-like reactions.[16] Metal-free carbon-based materials is another low-cost option.[17,18] Carbon is highly conductive, cheap and possessing tunable physicochemical properties.[19] However, even the best-performing carbons still have modest ORR and OER performance in non-alkaline ZABs.[14] An effective strategy to enhance their electrocatalytic properties is doping with nitrogen.[20] While N-doped carbons were tested in alkaline Zn–air cells,[21–24] the effects of doping on the performance in non-alkaline ZABs have remained unexplored.

An attractive approach for synthesizing carbon-based electrocatalysts is self-templating.[25–29] It involves pyrolysis of a metal–organic salt, during which organic moieties are carbonized and inorganic particles form inside the resulting carbon matrix, acting as a template which is then washed away. This is a simple and scalable method that produces hierarchically

[a] *Department of Chemistry and BINA – BIU Center for Nanotechnology and Advanced Materials, Bar-Ilan University, Ramat-Gan 5290002, Israel. E-mail: kapaevr@biu.ac.il, malachi.noked@biu.ac.il*

[b] *Schulich Faculty of Chemistry, the Resnick Sustainability Center for Catalysis, and the Grand Technion Energy Program Technion, Israel Institute of Technology, Technion City, Haifa 3200003, Israel*

[c] *R&D Division, Nichia Corporation, 491 Oka, Kaminaka, Anan, Tokushima 774-8601, Japan*

† Electronic supplementary information (ESI) available. See DOI: https://doi.org/10.1039/d3ya00560g

porous materials with high specific surface area, which is important because high concentration of catalytically active sites is required for fast ORR/OER. With this approach, nitrogen doping can be implemented simply by using nitrogen-containing organic ligands, such as nitrilotriacetic acid.[26–28] In this work, we study ORR/OER performance of undoped vs. N-doped self-templated carbons in near-neutral electrolytes and evaluate their performance in non-alkaline ZABs.

Results and discussion

Nitrogen-doped carbons were synthesized by pyrolyzing magnesium or barium salts of nitrilotriacetic acid, followed by treatment with HCl to remove carbonates. The resulting materials were designated as MgNC and BaNC, respectively. To understand the effects of nitrogen doping, we employed two types of nitrogen-free reference materials. The first one is C800, which was obtained via a similar self-templating approach using barium trimesate (salt of benzene-1,2,3-tricarboxylic acid) as the precursor.[30] The second one is Ketjenblack EC600JD, which has nearly the best ORR/OER performance in non-alkaline Zn–air cells among commercially available carbons.[14]

According to SEM, all materials synthesized using a self-templated approach have a similar morphology, consisting of micron-sized porous particles (Fig. 1a). Specifically, the particles of MgNC and BaNC contain arrays of roughly spherical pores with diameters of 10–20 nm and 30–40 nm, respectively. Larger pores ($\geq$100 nm) are observed for C800 in the SEM images. At the same time, EC600JD consists of aggregated 30–50 nm primary particles.

BET surface area for all materials is measured to be within a relatively narrow range of 1100–1370 m^2 g^{-1} (Fig. 1b), being higher for C800 (1294 m^2 g^{-1}) and EC600JD (1364 m^2 g^{-1}). Derived pore size distributions (Fig. 1c) are similar for C800, EC600JD and MgNC, revealing the presence of micropores (<2 nm) and mesopores (2–20 nm). While containing pores in the 0.5–8 nm range, BaNC has a fraction of larger mesopores compared to other materials (20–50 nm), in accordance with the SEM images.

According to XPS, nitrogen is present in MgNC and BaNC while absent in the reference materials (Fig. 1d). The ratio between different types of nitrogen is similar for MgNC and BaNC, as follows from N1s XPS signal deconvolution. For both materials, the most intense peak at 401.0 eV (N2) corresponds to graphitic nitrogens, a weaker peak at 398.3 eV (N1) corresponds to pyridinic nitrogens, and a minor peak at 405 eV (N3) is assigned to pyridinic oxides.[31–33] O1s XPS profiles are similar for C800, MgNC and BaNC (Fig. 1e). The peak at 533.2 eV (O2), which has higher intensity, can be assigned to C–O groups, while the peak at 532 eV (O1) corresponds to C=O moieties.[34,35] EC600JD has a lower content of C=O groups compared to the self-templated carbons. Overall oxygen content according to XPS is similar for C800 (6.8% at) and BaNC (6.1% at) and is slightly lower for EC600JD (3.9% at) and MgNC (3.6% at).

Self-templated carbons have only trace amounts of group II elements after washing with HCl. Optical emission spectroscopy with inductively coupled plasma (ICP-OES) analysis shows that barium content is 0.95% wt for C800 and 0.85% wt for BaNC, while MgNC contains 0.11% wt of magnesium. Unlike transition metals or platinum group elements, Ba and Mg are not catalytically active towards ORR/OER. Main group elements lack the combination of empty and filled host orbitals that are required for enabling catalytic redox processes.[36,37] Therefore, their trace amounts should not affect the material performance.

Raman spectra of C800, MgNC and BaNC are almost identical (Fig. 1f). They have highly intensive D1 (1350 cm^{-1}), D2 (1525 cm^{-1}) and D3 (1200 cm^{-1}) bands, which correspond to disordered domains of carbon,[38–40] while the G band (1600 cm^{-1}), which corresponds to graphitic domains, is relatively weak. For EC600JD, G/D1 band ratio is also low, but the D2 and D3 features are much less intensive. According to literature, D2 band corresponds to amorphous domains, while D3 band can be assigned to disordered graphitic lattice, grafted aliphatic moieties, polyene-like structures, or ionic impurities.[38–40] To summarize, all materials have low graphitization degree, but EC600JD has a less disordered structure than carbons obtained via the self-templating approach.

Overall, the characterization data show that C800, BaNC and MgNC have similar key properties, such as morphology, BET surface area and local chemical ordering. Since the main distinction between MgNC and C800 is the content of nitrogen, it can be suggested that any major differences in the ORR/OER performance are defined by catalytic activity of nitrogen-based sites. EC600JD can be used as an additional reference material, which performance in comparison to other types of carbon (graphene, nanotubes, nanofibers, activated carbon, etc.) was defined previously in non-alkaline Zn–air batteries.[14]

To study the kinetics of ORR and OER in near-neutral media, we performed electrochemical tests in phosphate buffer solution (PBS) with pH = 6.0. For all selected materials, cyclic voltammograms (CVs) measured with O_2-saturated PBS show features of oxygen reduction, while the CV response is purely capacitive when N_2-saturated electrolyte is employed (Fig. S1, ESI†). The electrode double-layer capacitance, which was calculated from the non-faradaic CV currents (Fig. S2, ESI†), is similar for C800, EC600JD and MgNC (2.4–2.6 mF cm^{-2}) and is lower for BaNC (1.6 mF cm^{-2}). Both CVs and linear sweep voltammograms (LSVs) measured using a rotating disk electrode (RDE) reveal that the ORR overpotentials are substantially lower for N-doped carbons compared to EC600JD and C800 (Fig. 2a and Fig. S1, ESI†). Koutecký-Levich analysis of the RDE data indicates that the ORR electron transfer numbers are also higher for the N-doped materials (Fig. S3, ESI†). This is in accordance with rotating ring-disk electrode (RRDE) measurements, which show higher contributions of four-electron O_2 reduction pathway for BaNC and MgNC (Fig. 2b and Fig. S4, ESI†).[28] However, no improvements of the OER performance are observed for the N-doped carbons compared to nitrogen-free benchmark C800 (Fig. 2c).

The materials were tested in Zn–air cells with 1 M $ZnSO_4$ (pH $\sim$ 3.9)[41] or 1 M $Zn(OAc)_2$ (pH $\sim$ 5.6)[41] solutions as the electrolytes. Discharge polarization curves (Fig. S5, ESI†) demonstrate superior ORR performance of BaNC and MgNC,
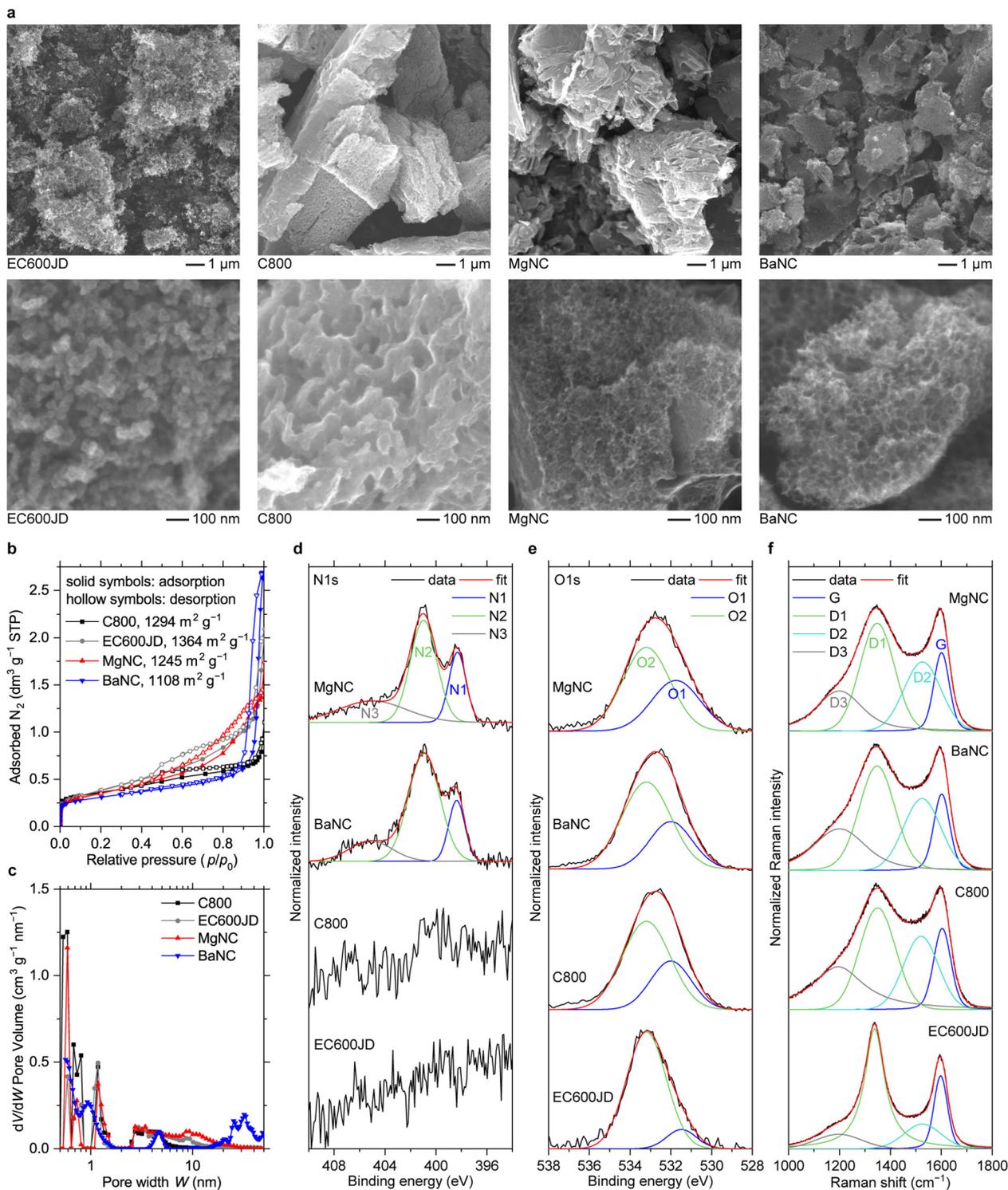
Fig. 1 Characterization of carbons: (a) SEM images; (b) N_2 adsorption isotherms (solid symbols), desorption isotherms (hollow symbols) and BET surface areas; (c) pore size distributions (V – volume, W – pore width); (d) N1s XPS; (e) O1s XPS; (f) Raman spectra.

with the peak power reaching 24.6 and 28.0 mW cm^{-2}, respectively. For comparison, the peak power values for EC600JD and C800 are only 9.2 and 12.1 mW cm^{-2}, respectively. Galvanostatic cycling of the Zn–air cells at 0.1 and 1 mA cm^{-2} reveals the same trend (Fig. 3): nitrogen-doped carbons have superior

ORR performance compared to the nitrogen-free benchmarks, as follows from higher discharge voltages of the batteries. However, no decrease of the charge voltages is observed for MgNC or BaNC in comparison to C800, indicating that the nitrogen-based sites have low catalytic activity towards OER.
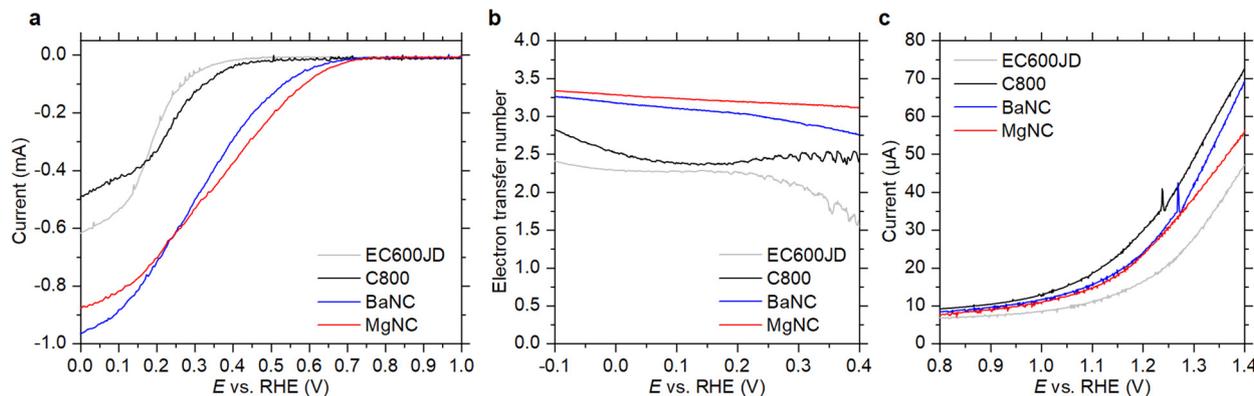
Fig. 2 Catalytic performance of carbons measured with rotating disk electrodes in O_2-saturated PBS (pH = 6.0): (a) ORR voltammograms at 1600 rpm; (b) ORR electron transfer numbers derived from the RRDE measurements; (c) OER voltammograms.

These results are in accordance with the RDE measurements in phosphate buffer solution (Fig. 2). Overall, using MgNC and BaNC in non-alkaline ZABs enhances the roundtrip energy efficiency compared to previously reported carbon materials (Table S1, ESI†). Based on the recent experimental and theoretical studies,[42–44] it is anticipated that pyridinic nitrogens have the highest catalytic activity towards ORR. Therefore, it might be suggested that increasing the content of pyridinic nitrogens might further enhance the material performance.

Notably, micron-sized particles of hierarchically porous carbons have better or comparable ORR performance than the nanosized EC600JD in non-alkaline ZABs. This is in contrast to microporous carbons with micron-sized particles, such as YP50F or YP80,[14] which despite their large specific surface area (>1600 m^2 g^{-1}) have poor ORR performance at 1 mA cm^{-2} in exactly the same Zn–air cell setup. This indicates that the pore size plays a critical role in oxygen reduction kinetics. Apparently, micropores (<2 nm) are too small to ensure fast oxygen diffusion within the big particles, so larger pores are required to ensure fast supply of O_2 to the catalytically active sites.

Previous studies suggest that there is an optimal pore size for selective four-electron ORR, which is related to confinement of peroxide species within the pores.[28] Smaller mesopores allow trapping of the intermediate peroxide products, so they can be further reduced within the pores. However, if the pores are too large then the peroxides diffuse away, leading to a decrease of electron transfer number. For this reason, the ORR performance is better for MgNC compared to BaNC in alkaline electrolytes.[28] Since the same trend is observed in non-alkaline media, it might be concluded that the same confinement effect is relevant at near-neutral pH values.

While the initial ORR performance of N-doped carbons in non-alkaline media is promising, the ORR overpotentials tend to increase upon cycling (Fig. 3). One of the main degradation mechanisms of carbon materials is their oxidation during OER, which takes place in non-alkaline ZABs.[45] We compared the corrosion rate of C800, MgNC and BaNC by monitoring CO_2 levels within the cells using online electrochemical mass-spectrometry (OEMS). Observed CO_2 evolution rates are similar for all materials (Fig. S6, ESI†), indicating that nitrogen doping

does not improve corrosion resistance of carbon. Further studies are needed to develop corrosion-resistant catalysts for ZABs, either by applying protective coatings or decreasing the OER overpotentials.[45]

Several studies suggested that oxygen doping, such as functionalization with C=O groups, can enhance the OER kinetics in alkaline media.[44,46,47] However, no decrease of the OER overpotentials is observed upon battery cycling (Fig. 3), although carbon oxidation during the OER leads to formation of C–O/C=O functional groups at the surface.[45,48] Furthermore, MgNC and BaNC have similar OER performance, although the oxygen content is lower for MgNC. This indicates that the oxygen functionalization degree is not the key factor which determines the OER performance in non-alkaline ZABs. To improve the oxygen evolution kinetics, doping with other elements might be required.

Conclusions

To summarize, this study shows that nitrogen doping of carbon leads to a substantial improvement of ORR kinetics in non-alkaline Zn–air batteries. Hierarchically porous N-doped carbons (MgNC and BaNC) outperform their nitrogen-free analog (C800), as well as the best commercially available nitrogen-free carbons. At the same time, nitrogen doping does not improve the OER performance or the carbon corrosion rate, indicating that other types of catalytically active sites need to be added to the materials to promote fast oxygen evolution in near-neutral media. Overall, nitrogen-doped carbons can serve as promising support materials for non-alkaline Zn–air battery cathodes.

Experimental

Materials

Barium acetate (Riedel-de Haen, 99%), barium carbonate basic (Acros Organics), benzene-1,3,5-tricarboxylic acid (Sigma-Aldrich, 95%), ethanol (BIOLAB, 96% cp), isopropanol (CARLO ERBA reagents, HPLC PLUS Gradient grade), Ketjenblack EC600JD (Fuel Cell Store), magnesium carbonate basic (Acros Organics),
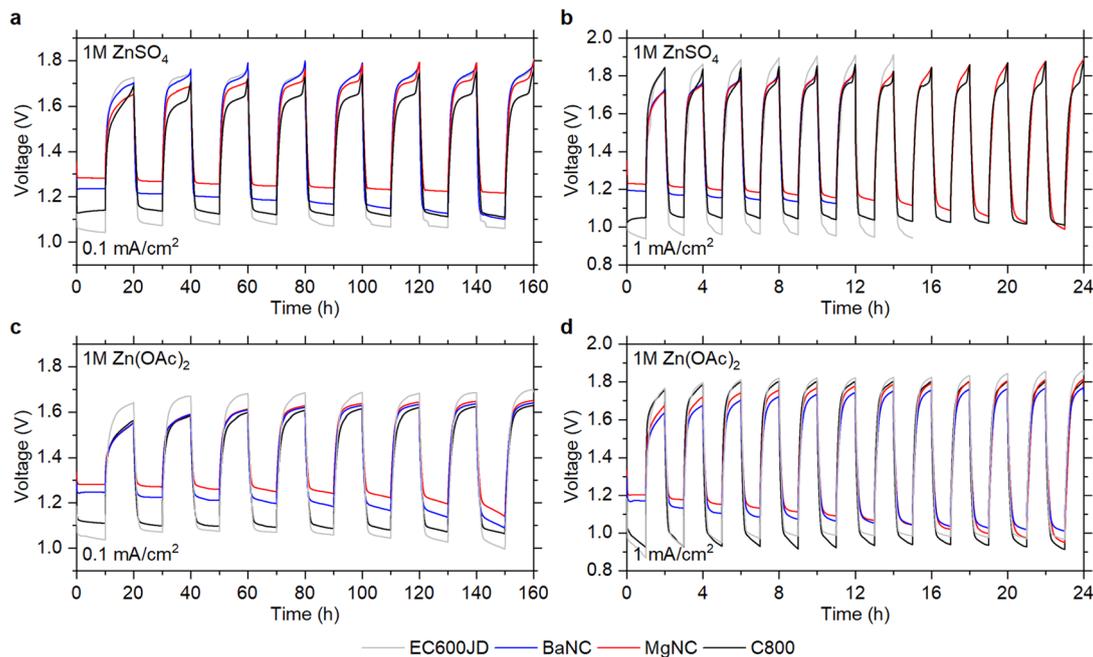
Fig. 3 Voltage profiles during galvanostatic cycling of Zn–air cells at (a) and (c) 0.1 mA cm^{-2} and (b) and (d) 1 mA cm^{-2} with (a) and (b) 1 M ZnSO$_4$ and (c) and (d) 1 M Zn(OAc)$_2$ as electrolytes.

N,N-dimethylformamide (Biolab, AR), Nafion (Alfa Aesar, 5% w/w in water/1-propanol), nitrilotriacetic acid (Acros Organics, 99%), polytetrafluoroethylene preparation (Sigma Aldrich, 60% dispersion in water), Sigracet 39BB carbon paper (Fuel Cell Store), Whatman glass microfiber separators (GF/A grade), zinc foil (Grillo, degreased, ≥99.95%, 80 μm thickness), zinc acetate dihydrate (Sigma Aldrich, ACS reagent, ≥98%), zinc sulfate heptahydrate (Sigma Aldrich, puriss., ACS reagent, ≥99.5%).

Synthesis of C800

Barium trimesate precursor was prepared from a solution of 0.105 mol benzene-1,3,5-tricarboxylic acid and 0.105 mol barium acetate in 5 L of double deionized water at 78 °C. Precipitation of salt occurred immediately with the addition of barium acetate. The suspension was decanted, and the salt was dried at 50 °C overnight. The salt was pyrolyzed in a quartz boat under argon flow at 800 °C for 1 h with a ramp rate of 5 °C min^{-1}. This yielded a carbon loaded with BaCO$_3$ nanoparticles, denoted as BaCO$_3$@C800. The BaCO$_3$ was washed out by overnight stirring in 1 M HCl, followed by washing with 1 L of double deionized water. The resulting material was dried overnight at 50 °C.

Synthesis of MgNC and BaNC

Ba/Mg-NTA precursors were prepared from a solution of 180 mmol of nitrilotriacetic acid and 144 mmol of barium carbonate basic (for Ba-NTA) or 207 mmol of magnesium carbonate basic (for Mg-NTA) in 500 mL of double deionized water at 78 °C. Precipitation of salt occurred after addition of 1.5 L of ethanol. The suspensions were cooled to ~40 °C in an ice bath for 2 h for further precipitation. The suspensions were

decanted, and the salts were dried at 50 °C overnight. The salts were pyrolyzed in a quartz boat under argon flow at 800 °C for 1 h with a ramp rate of 5 °C min^{-1}. The resulting materials were loaded with BaCO$_3$ or MgO nanoparticles. The nanoparticles were washed out by overnight stirring in 1 M HCl, followed by washing with 1 L of double deionized water. The carbons were dried overnight at 50 °C.

Characterization

Scanning electron microscopy images were acquired with an FEI Magellan 400L high-resolution scanning electron microscope. X-ray photoelectron spectra measurements were carried out using a PHI 5600 Multi-Technique System with an Al Kα monochromatic source (1486.6 eV); XPS peaks were calibrated by setting the binding energy of the major C1s peak to 285.0 eV; three measurements were made for each sample to check reproducibility. Raman spectra were measured with a Horiba LabRAM Soleil Raman microscope; the laser excitation wavelength was 532 nm, the laser power was 0.79 mW, the grating was 1800 lines mm^{-1}; five measurements were performed for each sample to check reproducibility. N$_2$ adsorption–desorption isotherms at 77 K were measured using a Quantachrome Autosorb iQ instrument. The samples were vacuum-dried at 200 °C for 10 h before the measurements. BET specific surface was calculated with BETSI software.[49] Pore size distributions were derived using isotherm fitting with a quenched solid state density functional theory (QSDFT) model (N$_2$/carbon, 77 K, slit-shaped pores, equilibrium measurements). For ICP-OES measurements, the materials (~1 mg) were dissolved in 1 mL of concentrated HNO$_3$; the elemental analysis was then performed with SPECTRO Arcos FHX22 MultiView plasma.

Electrochemistry with rotating disk electrodes

To preprate the electrodes, inks of the carbon catalysts were prepared by adding 1 mg of carbon to 1 mL N,N-dimethylformamide and 40 µL of Nafion suspension (5% w/w in water/1-propanol). The inks were sonicated for 30 min, and 10 µL of the inks were drop-cast on a polished rotating ring disk electrode (Pine E7R9 glassy carbon disk φ = 5.61 mm, Pt ring, 37% collection efficiency), the resulting electrodes were dried for 45 min at 50 °C. Carbon loading of the electrodes was 0.04 mg cm^{-2}.

ORR voltammograms were recorded in a three-electrode glass cell using a BioLogic VSP potentiostat. The counter electrode was a graphite rod, reference electrode was a HydroFlex RHE, and the supporting electrolyte was 0.1 M potassium phosphate buffer solution (pH = 6.0 at 25 °C). Measurements were carried out in N$_2$ (99.999%) purged cell for baseline and O$_2$ purged cell for ORR. Potentials were applied using an automatic 80% IR correction. Cyclic voltammograms (CVs) and linear sweep voltammograms (LSVs) were collected with a scan rate of 10 mV s^{-1} unless stated otherwise.

Electrode preparation for Zn–air cells

C800, MgNC or BaNC (150 mg) were mixed in an agate mortar with water (300 µL) and polytetrafluoroethylene (15 mg, as a water-based dispersion), followed by mixing of these components with isopropanol (750 µL). The resulting slurries were tape-cast onto hydrophobic carbon paper (Sigracet 39BB). The electrodes were oven-dried at 100 °C for 15–30 min, then roll-pressed and cut into disks (d = 11 mm). The procedure was similar for Ketjenblack EC600JD, but higher amounts of water (600 µL) and isopropanol (1500 µL) were used per 150 mg of carbon because the material absorbs a lot of solvent without forming a processable slurries. The loading of carbon blacks in the resulting electrodes was from 9 to 10 mg cm^{-2}.

Zn–air cell assembling and electrochemistry

Previously reported custom-made two-electrode cells[14,45] were assembled in ambient air for assessing the electrochemical performance of carbons in ZABs. These cells accommodate ~16 mL of air. Zn foil disks (d = 13 mm) were used as the anodes, glass fiber disks (d = 21 mm) were used as the separators, 120 µL of electrolyte (1 M ZnSO$_4$ or 1 M Zn(OAc)$_2$ in water) was added to the cells. The cells were kept at an open-circuit voltage for 5 h before cycling. Galvanostatic cycling of the cells and polarization studies (LSV at 10 mV s^{-1}) were performed at room temperature using BioLogic VMP3 or Neware BTS4000.

OEMS measurements

Gas composition analysis was performed using an HPR-20 eight-channel mass spectrometer (Hiden Analytical). Signal acquisition was performed with an SEM detector. The OEMS capillaries were connected to the cell outlets in an air-tight way using Swagelok fittings with PTFE ferrules.

Author contributions

R. R. K., M. N., Y. S. and D. E. designed the study. R. R. K. measured Raman spectra and performed studies in Zn–air cells, including OEMS experiments. Y. S. synthesized the materials and performed electrochemical tests in phosphate buffer solution. M. S. measured XPS, M. S. and R. R. K. analyzed the XPS data. A. O. acquired SEM images and prepared the samples for ICP-OES measurements. R. R. K. wrote the manuscript with contributions from other authors.

Conflicts of interest

There are no conflicts to declare.

Acknowledgements

References

1 K. W. Leong, Y. Wang, M. Ni, W. Pan, S. Luo and D. Y. C. Leung, Renewable Sustainable Energy Rev., 2022, 154, 111771.

2 J. W. Choi and D. Aurbach, Nat. Rev. Mater., 2016, 1, 16013.

3 J. Liu, J.-G. Zhang, Z. Yang, J. P. Lemmon, C. Imhoff, G. L. Graff, L. Li, J. Hu, C. Wang, J. Xiao, G. Xia, V. V. Viswanathan, S. Baskaran, V. Sprenkle, X. Li, Y. Shao and B. Schwenzer, Adv. Funct. Mater., 2013, 23, 929–946.

4 H. D. Yoo, E. Markevich, G. Salitra, D. Sharon and D. Aurbach, Mater. Today, 2014, 17, 110–121.

5 J. Pan, Y. Y. Xu, H. Yang, Z. Dong, H. Liu and B. Y. Xia, Adv. Sci., 2018, 5, 1700691.

6 X. X. Wang, X. Yang, H. Liu, T. Han, J. Hu, H. Li and G. Wu, Small Struct., 2022, 3, 2100103.

7 J. Zhang, Q. Zhou, Y. Tang, L. Zhang and Y. Li, Chem. Sci., 2019, 10, 8924–8929.

8 J. Yi, P. Liang, X. Liu, K. Wu, Y. Liu, Y. Wang, Y. Xia and J. Zhang, Energy Environ. Sci., 2018, 11, 3075–3095.

9 S. Zhao, T. Liu, J. Wang, I. Temitope Bello, Y. Zuo, M. Wei, K. Wang, K. K. S. Lau and M. Ni, Chem. Eng. J., 2022, 450, 138207.

10 W. Sun, V. Küpers, F. Wang, P. Bieker and M. Winter, Angew. Chem., Int. Ed., 2022, 61, e202207353.

11 C. Li, L. Wang, J. Zhang, D. Zhang, J. Du, Y. Yao and G. Hong, Energy Storage Mater., 2022, 44, 104–135.

12 W. Sun, F. Wang, B. Zhang, M. Y. Zhang, V. Kupers, X. Ji, C. Theile, P. Bieker, K. Xu, C. S. Wang and M. Winter, Science, 2021, 371, 46–51.

13 C. Wang, J. Li, Z. Zhou, Y. Pan, Z. Yu, Z. Pei, S. Zhao, L. Wei and Y. Chen, Energy Chem., 2021, 3, 100055.

14 R. R. Kapaev, A. Ohayon, M. Sonoo, J. Tzadikov, M. Shalom and M. Noked, Electrochim. Acta, 2023, 456, 142462.

15 S. Das, A. Kundu, T. Kuila and N. C. Murmu, Energy Storage Mater., 2023, 61, 102890.

16 G. Bae, M. W. Chung, S. G. Ji, F. Jaouen and C. H. Choi, ACS Catal., 2020, 10, 8485–8495.

17 J. Zhang, Z. Xia and L. Dai, Sci. Adv., 2015, 1, e1500564.

18 P. Trogadas, T. F. Fuller and P. Strasser, Carbon, 2014, 75, 5–42.

19 J. Wang, H. Kong, J. Zhang, Y. Hao, Z. Shao and F. Ciucci, *Prog. Mater. Sci.*, 2021, **116**, 100717.

20 K. Gao, B. Wang, L. Tao, B. V. Cunning, Z. Zhang, S. Wang, R. S. Ruoff and L. Qu, *Adv. Mater.*, 2019, **31**, 1805121.

21 X. Lu, L. Ge, P. Yang, O. Levin, V. Kondratiev, Z. Qu, L. Liu, J. Zhang and M. An, *Appl. Surf. Sci.*, 2021, **562**, 150114.

22 Y. Deng, H. Zhang, Y. Lin, Q. Ying, F. Yu and Y. Yang, *Dalton Trans.*, 2022, **51**, 18152–18158.

23 P. Wei, X. Li, Z. He, X. Sun, Q. Liang, Z. Wang, C. Fang, Q. Li, H. Yang, J. Han and Y. Huang, *Chem. Eng. J.*, 2021, **422**, 130134.

24 W. Li, J. Wang, C. Jia, J. Chen, Z. Wen and A. Huang, *J. Colloid Interface Sci.*, 2023, **650**, 275–283.

25 M. Sevilla and A. B. Fuertes, *J. Mater. Chem. A*, 2013, **1**, 13738–13741.

26 D. Eisenberg, W. Stroek, N. J. Geels, C. S. Sandu, A. Heller, N. Yan and G. Rothenberg, *Chem. – Eur. J.*, 2016, **22**, 501–505.

27 D. Eisenberg, W. Stroek, N. J. Geels, S. Tanase, M. Ferbinteanu, S. J. Teat, P. Mettraux, N. Yan and G. Rothenberg, *Phys. Chem. Chem. Phys.*, 2016, **18**, 20778–20783.

28 E. M. Farber, K. Ojha, T. Y. Burshtein, L. Hasson and D. Eisenberg, *Mater. Adv.*, 2020, **1**, 20–33.

29 G. A. Ferrero, N. Diez, M. Sevilla and A. B. Fuertes, *Microporous Mesoporous Mater.*, 2019, **278**, 280–288.

30 Y. Shahaf, A. Mahammed, A. Raslin, A. Kumar, E. M. Farber, Z. Gross and D. Eisenberg, *ChemElectroChem*, 2022, **9**, e202200045.

31 A. Vesel, R. Zaplotnik, G. Primc and M. Mozetič, *Nanomaterials*, 2020, **10**, 2286.

32 C. Xie, L. Lin, L. Huang, Z. Wang, Z. Jiang, Z. Zhang and B. Han, *Nat. Commun.*, 2021, **12**, 4823.

33 S. N. Faisal, E. Haque, N. Noorbehesht, W. Zhang, A. T. Harris, T. L. Church and A. I. Minett, *RSC Adv.*, 2017, **7**, 17950–17958.

34 M. Zhu, J. Lan, X. Zhang, G. Sui and X. Yang, *New J. Chem.*, 2017, **41**, 4281–4285.

35 F. G. Pacheco, A. A. C. Cotta, H. F. Gorgulho, A. P. Santos, W. A. A. Macedo and C. A. Furtado, *Appl. Surf. Sci.*, 2015, **357**, 1015–1023.

36 B. Zhu, K. Qiu, C. Shang and Z. Guo, *J. Mater. Chem. A*, 2015, **3**, 5212–5222.

37 M.-A. Légaré, G. Bélanger-Chabot, R. D. Dewhurst, E. Welz, I. Krummenacher, B. Engels and H. Braunschweig, *Science*, 2018, **359**, 896–900.

38 M. Pawlyta, J.-N. Rouzaud and S. Duber, *Carbon*, 2015, **84**, 479–490.

39 T. Jawhari, A. Roid and J. Casado, *Carbon*, 1995, **33**, 1561–1565.

40 A. Sadezky, H. Muckenhuber, H. Grothe, R. Niessner and U. Pöschl, *Carbon*, 2005, **43**, 1731–1742.

41 W. Yuan, X. Nie, G. Ma, M. Liu, Y. Wang, S. Shen and N. Zhang, *Angew. Chem., Int. Ed.*, 2023, **62**, e202218386.

42 S. K. Singh, K. Takeyasu and J. Nakamura, *Adv. Mater.*, 2019, **31**, 1804297.

43 L. Liu, G. Zeng, J. Chen, L. Bi, L. Dai and Z. Wen, *Nano Energy*, 2018, **49**, 393–402.

44 H. B. Yang, J. Miao, S.-F. Hung, J. Chen, H. B. Tao, X. Wang, L. Zhang, R. Chen, J. Gao, H. M. Chen, L. Dai and B. Liu, *Sci. Adv.*, 2016, **2**, e1501122.

45 R. R. Kapaev and M. Noked, *Chem. Commun.*, 2023, **59**, 9856–9859.

46 X. Lu, W.-L. Yim, B. H. R. Suryanto and C. Zhao, *J. Am. Chem. Soc.*, 2015, **137**, 2901–2907.

47 Z. Pei, H. Li, Y. Huang, Q. Xue, Y. Huang, M. Zhu, Z. Wang and C. Zhi, *Energy Environ. Sci.*, 2017, **10**, 742–749.

48 Y. Yi, G. Weinberg, M. Prenzel, M. Greiner, S. Heumann, S. Becker and R. Schlögl, *Catal. Today*, 2017, **295**, 32–40.

49 J. W. M. Osterrieth, J. Rampersad, D. Madden, N. Rampal, L. Skoric, B. Connolly, M. D. Allendorf, V. Stavila, J. L. Snider, R. Ameloot, J. Marreiros, C. Ania, D. Azevedo, E. Vilarrasa-Garcia, B. F. Santos, X. H. Bu, Z. Chang, H. Bunzen, N. R. Champness, S. L. Griffin, B. L. Chen, R. B. Lin, B. Coasne, S. Cohen, J. C. Moreton, Y. J. Colon, L. J. Chen, R. Clowes, F. X. Coudert, Y. Cui, B. Hou, D. M. D'Alessandro, P. W. Doheny, M. Dinca, C. Y. Sun, C. Doonan, M. T. Huxley, J. D. Evans, P. Falcaro, R. Ricco, O. Farha, K. B. Idrees, T. Islamoglu, P. Y. Feng, H. J. Yang, R. S. Forgan, D. Bara, S. Furukawa, E. Sanchez, J. Gascon, S. Telalovic, S. K. Ghosh, S. Mukherjee, M. R. Hill, M. M. Sadiq, P. Horcajada, P. Salcedo-Abraira, K. Kaneko, R. Kukobat, J. Kenvin, S. Keskin, S. Kitagawa, K. I. Otake, R. P. Lively, S. J. A. DeWitt, P. Llewellyn, B. V. Lotsch, S. T. Emmerling, A. M. Putz, C. Marti-Gastaldo, N. M. Padial, J. Garcia-Martinez, N. Linares, D. Maspoch, J. A. S. del Pino, P. Moghadam, R. Oktavian, R. E. Morris, P. S. Wheatley, J. Navarro, C. Petit, D. Danaci, M. J. Rosseinsky, A. P. Katsoulidis, M. Schroder, X. Han, S. H. Yang, C. Serre, G. Mouchaham, D. S. Sholl, R. Thyagarajan, D. Siderius, R. Q. Snurr, R. B. Goncalves, S. Telfer, S. J. Lee, V. P. Ting, J. L. Rowlandson, T. Uemura, T. Liyuka, M. A. van derVeen, D. Rega, V. Van Speybroeck, S. M. J. Rogge, A. Lamaire, K. S. Walton, L. W. Bingel, S. Wuttke, J. Andreo, O. Yaghi, B. Zhang, C. T. Yavuz, T. S. Nguyen, F. Zamora, C. Montoro, H. C. Zhou, A. Kirchon and D. Fairen-Jimenez, *Adv. Mater.*, 2022, **34**, 2201502.